J. Iron Steel Res. Int. (2020) 27:440–450
https://doi.org/10.1007/s42243-019-00317-8

ORIGINAL PAPER

Microstructure and mechanical properties of hot-rolled low-carbon steel containing Ti–Ca oxide particles: a comparison between base metal and HAZ

Chao Wang[1] · Xin Wang[1] · Jian Kang[1] · Guo Yuan[1] · Guo-dong Wang[1]

Received: 15 February 2019 / Revised: 6 May 2019 / Accepted: 15 May 2019 / Published online: 28 September 2019

Abstract
The effect of inclusion-induced nucleation on hot-rolled steel base metal was evaluated in comparison with welding heat-affected zone (HAZ). Microstructure and mechanical properties of hot-rolled low-carbon steel containing Ti–Ca oxide particles were studied. The results showed that inclusions in Ti–Ca deoxidized steel distributed dispersely and were effective for intragranular acicular ferrite nucleation. Under hot rolling and controlled cooling conditions, microstructure in steel base metal was significantly refined and mainly consisted of acicular ferrite and intragranular bainite, which exhibited higher strength and excellent toughness. The microstructural evolution behavior followed the process that acicular ferrite plates divided the austenite grain, intragranular bainite packets formed between interlocking acicular ferrite plates, and the remaining austenite decomposed into fine polygonal ferrite grains. The resultant complex microstructure improved the impact toughness significantly. By comparison, in HAZ microstructure, laminar grain boundary ferrite having similar crystallography orientation showed adverse effect on toughness.

Keywords Low-carbon steel · Ti–Ca oxide · Hot rolling · Mechanical property · Acicular ferrite · Heat-affected zone

1 Introduction

Particle-stimulated nucleation is frequently used in improving steel microstructure and mechanical properties. One typical application is the grain refinement of steel weld metal and heat-affected zone [1–3]. Acicular ferrite (AF) exhibits satisfactory combination of strength and toughness due to its interlocking morphology. It is also the preferred microstructure in coarse-grained heat-affected zone (CGHAZ) under large welding heat input, where detrimental ferrite side plates (FSP) are usually formed [4, 5]. A number of researches have been carried out to enhance HAZ toughness by optimizing inclusion composition and distribution [6–9]. Ti oxide, Ti_2O_3 in particular, exhibits remarkable ability for AF nucleation and has received greatest interest [10]. In order to promote a disperse distribution of fine-sized inclusions, strong deoxidant such as Al, Mg, Zr or Ca is usually added together with Ti [11–13]. Besides, many other researches focused on factors influencing AF nucleation ability such as steel composition, inclusion size and interface coherence [14, 15]. In a sense, the above researches mainly considered microstructural evolution under static conditions, where materials thermo-mechanical processing was not taken into account.

Thermo-mechanical processing involves austenite hot deformation and controlled cooling. Research showed that austenite deformation conditions have evident influence on AF formation of low-carbon steel containing Ti oxide [16]. Under high holding temperature and slow cooling rate, microstructure of heavy section steel was refined by Ti oxide particles [17]. Proper cooling process was also in favor of AF microstructure formation [18]. Some research work also investigated particle evolution behavior during thermo-mechanical process [19, 20]. Oxide or oxy-sulfide particle composition did not change much during the hot-working process. However, for steels using sulfide or

✉ Guo Yuan
yuanguo_neu@163.com

[1] The State Key Laboratory of Rolling and Automation, Northeastern University, Shenyang 110819, Liaoning, China

carbo-nitride as nucleating particles, precipitation during thermo-mechanical process was necessary [21, 22].

For weldable high strength low alloy (HSLA) steels, thermo-mechanical controlled process (TMCP) is widely used to improve steel properties. By TMCP, low-temperature deformation in austenite region and accelerated cooling result in significant microstructure refinement [23]. However, for certain products such as heavy plates, heavy sections, hot-rolled bars and seamless pipes, TMCP cannot be appropriately applied because of their special section shapes. Austenite grains in these steel products grow such that coarse microstructure is usually formed in spite of accelerated cooling. The particle-stimulated nucleation tends to take place in large-sized austenite grains, and thus it shows special advantage for these products. However, microstructures and mechanical properties obtained by TMCP and particle-stimulated nucleation still lack comparative study. Moreover, the difference in transformation behaviors between hot-rolled base metal and welding HAZ need further understanding. In this study, low-carbon steels with and without effective Ti–Ca oxide particles were prepared. The steels were subjected to hot rolling and HAZ simulation, respectively. Characteristics of microstructure and mechanical properties under different conditions were analyzed.

2 Experimental procedure

Two experimental steels were melted in a laboratory 50-kg vacuum induction furnace and cast into ingots in a 20 kPa argon atmosphere. The basic composition of both steels was C 0.07, Si 0.21, Mn 1.75, S 0.004, P 0.01, and Fe balance (wt.%). One heat was deoxidized with master alloy containing Ti–Ca and marked as TC steel. The other heat was deoxidized by aluminum for comparison and marked as AL steel. In order to avoid the detrimental effect of non-metallic inclusions on steel ductility, the killing time before casting after deoxidant addition was controlled such that coarse inclusions were able to cluster and float up. At the same time, adequate fine oxide inclusions were kept in liquid steel as effective particles for microstructure refinement. The residual oxygen and deoxidant contents in steels were approximately O 0.003%, Ti 0.01%, Ca 0.002% and Al 0.02%, respectively. Almost all the oxide particles observed by scanning electron microscopy (SEM) during experiment were sized under 2 μm. Composition analysis by SEM energy-dispersive spectrometry (EDS) showed that Ti–Ca complex oxide and Al oxide were obtained in TC steel and AL steel, respectively, as expected. MnS was also frequently observed to precipitate on oxide particles.

The ingots were hot-forged into 80 mm × 80 mm square billets and then cut into steel samples and blocks for thermal cycle simulation and hot-rolling experiments. Austenite continuous cooling transformation (CCT) behavior was detected using Formastor-FII full-automatic transformation equipment. Cylinder samples of ϕ3 mm × 10 mm were heated at 10 °C/s to 1250 °C and held for 5 min. Then, the samples were cooled to 900 °C and subsequently cooled at different rates of 0.15–50 °C/s to ambient temperature. Dilation in sample length during cooling was determined. Finally, the samples were cross-sectioned and metallographically prepared for microstructure characterization.

Hot-rolling experiments were carried out on a laboratory rolling mill. Steel blocks were reheated to 1250 °C and held for 30 min, and then hot rolled into 20-mm-thick plates through 5 reversible rolling passes. The interpass operation was continuous, and the finish rolling temperature was between 1050 and 1100 °C. The hot plates were subsequently transferred to a water jet device and accelerated cooled from above 1000 °C to 600–650 °C at a rate of 10–20 °C/s and then cooled to ambient temperature in air. The hot-rolled steels were still designated as TC and AL plates, respectively. In addition, with the commonly used two-stage controlled rolling process, another plate of AL steel was rolled with a lower finishing temperature of 830 °C and similar cooling process as above. And the controlled rolled AL steel plate was designated as AL–cr plate. Tensile samples with gauge dimensions of 8 mm in diameter and 40 mm in length were machined in transverse direction of the plates. Charpy V-notch impact samples with standard dimensions of 10 mm × 10 mm × 55 mm were machined along rolling direction. Samples with dimensions of 11 mm × 11 mm × 55 mm were machined from TC and AL plates for HAZ simulation experiment. Coarse-grained HAZ for welding energy input of 200 kJ/cm was simulated on a MMS300 machine, during which the peak temperature was 1400 °C (staying for 5 s) and the cooling time from 800 to 500 °C ($t_{8/5}$) was 215 s. HAZ samples were then machined to standard dimensions for Charpy V-notch impact test at − 40 °C. Microstructure characterization was carried out using LEICA DMIRM optical microscope and FEI Quanta 600 SEM equipped with electron backscatter diffraction (EBSD) system.

3 Results and discussion

3.1 Continuous cooling transformation

Continuous cooling transformation diagrams of two steels are presented in Fig. 1, where A_{e1}, A_{e3} and A_{r3} points are 703, 827 and 748 °C, respectively. The corresponding microstructures are shown in Fig. 2. For the experimental cooling rates, the overall difference between two steels can

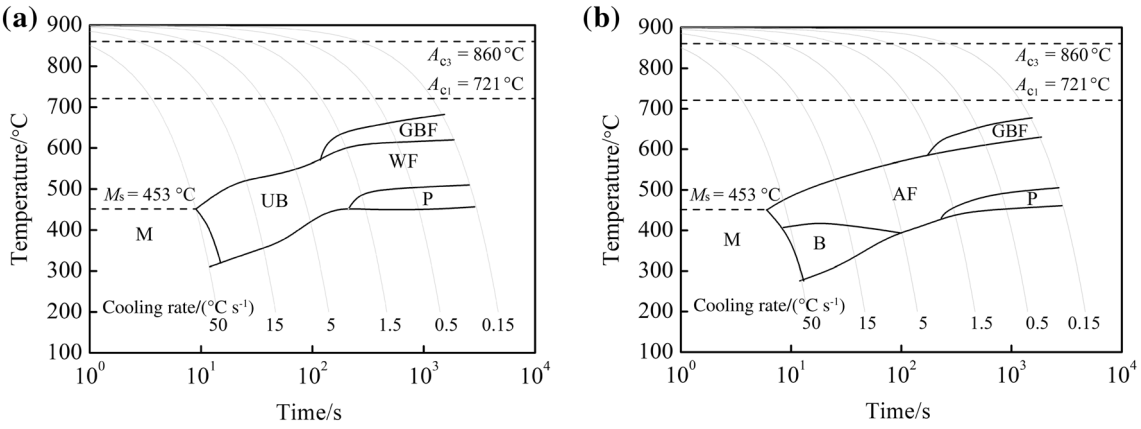

Fig. 1 CCT diagrams of AL steel (**a**) and TC steel (**b**) with austenization at 1250 °C. *P* Pearlite; *UB* upper bainite; *M* martensite; *GBF* grain boundary ferrite; *WF* Widmanstätten ferrite; *B* Bainite

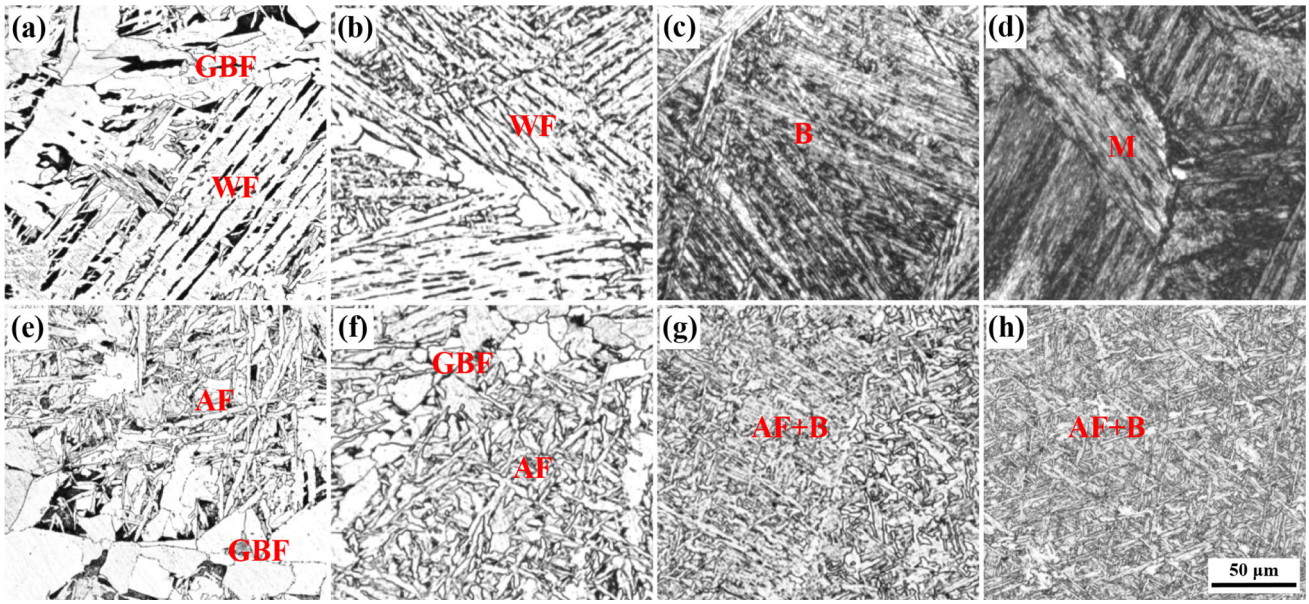

Fig. 2 Optical micrographs of AL steel (**a**–**d**) and TC steel (**e**–**h**) continuously cooled at 0.15 °C/s (**a**, **e**), 1.5 °C/s (**b**, **f**), 15 °C/s (**c**, **g**) and 50 °C/s (**d**, **h**)

be described as that microstructures growing from austenite grain boundaries were formed in AL steel, whereas intragranular transformation products were obtained in TC steel. For low cooling rates of 0.15–1.50 °C/s, GBF was formed in both steels. However, apparent morphological difference exists between the two types of ferrite. In AL steel, laminar ferrite grew along boundaries and readily promoted nucleation of WF or ferrite side plates (FSP), as shown in Fig. 2a, b. In TC steel, GBF grains were mostly polygonal and appeared inert for FSP nucleation, as shown in Fig. 2e, f. The different characteristics are related to GBF nucleation manner and its crystallography. Laminar GBF had near Kurdjumov–Sachs (K–S) relationship with one of neighboring austenite grains and could act as nucleating substrate for FSP. FSP growing from sympathetic nucleation had low-angle misorientation with GBF and K–S relationship with parent austenite [24]. Ferrite grains nucleating on precipitation particles at boundaries grew into a polygonal shape without special orientation relationship with austenite, and inhibited FSP from nucleating on the α/γ interface [25, 26]. Interior austenite then decomposed into acicular ferrite by intragranular nucleation instead. Thus, both the intergranular and intragranular reaction products were refined as a result of a distribution of favorable oxide particles in TC steel.

At a medium cooling rate of 5 °C/s, whole upper bainite and AF structure were obtained in AL steel and TC steel, respectively. As the cooling rate increased up to 50 °C/s, a microstructural transition from bainite to martensite could

be observed in AL steel, as shown in Fig. 2c, d. However, different types of multi-phase structure were formed for TC steel, as shown in Fig. 2g, h. AF plates still partially formed with cooling rates up to 50 °C/s, which segmented the austenite grain. Bainite or martensite packets formed within the regions between AF plates, resulting in much finer multi-phase structure. From the aspect of martensite formation tendency, the hardenability of TC steel decreased compared with that of AL steel. It is a common phenomenon that carbo-nitride precipitation in low alloy steels, such as NbC or VN precipitation [27, 28], could result in reduction in hardenability. It is obviously not the case for the present steels. On the other hand, oxygen content in weld metal can vary in a wide range and has a significant effect on WM microstructure and toughness [29]. Hardenability of WM decreased with the increase in oxygen content and oxide inclusion number [30]. The effective oxide particles in the present TC steel exhibited similar effect by stimulating AF nucleation even though the oxygen content was rather low.

Figure 3 shows a typical oxide particle promoting AF nucleation and its composition distribution. The particle is rich in Ti and Ca, with MnS precipitation on local surface. It could be simplified as Ti_2O_3·CaO·MnS for discussion. Each of the three constituents is favorable for stimulating AF nucleation. The effectiveness of Ti_2O_3 is generally attributed to the formation of Mn-depletion zone (MDZ) through Mn atoms absorption into Ti_2O_3 or MnS adherent precipitation. CaO formed in liquid steel has high solubility for sulfur and would promote MnS precipitation on its surface during cooling due to the decrease in sulfur solubility. These factors all contribute to MDZ development and strengthen AF-nucleating ability. Besides Ti_2O_3·CaO·MnS, other effective inclusion types containing Ti oxide were also observed, as presented in Fig. 4. Among the inclusions, Al_2O_3 was formed because of residual Al element in the alloy used.

3.2 As-rolled and simulated HAZ characteristics

Microstructures of hot-rolled and controlled cooled steel plates are presented in Fig. 5. Accelerated water cooling stopped above 600 °C and the following air cooling rate was about 0.5 °C/s for 20-mm-thick plates. For the high-temperature rolled steels, GBF was significantly suppressed with the controlled cooling process, as shown in Fig. 5a, b, and the intragranular structures also changed much from that without deformation. Coarse granular or lath bainite (GB/LB) sheaves were formed in AL steel plate (Fig. 5a, d). Complex microstructure was obtained in TC steel plate, which was comprised of acicular ferrite, polygonal or quasi-polygonal ferrite (PF/QPF), granular or lath bainite, and microphase of degenerated pearlite (DP) or martensite/austenite constituent (M/A), as shown in Fig. 5b, e, f. This type of microstructure is rather like that of HSLA steel produced by TMCP technology such as AF linepipe steel. Linepipe steels or Nb-microalloyed steels are generally subjected to heavy reduction in the austenite non-recrystallization region, resulting in significantly refined austenite grain size. In this experiment, austenite completely recrystallized at the high rolling temperature and grew into a coarse grain size of 50–100 μm. Thus, the microstructure refinement mainly depended on intragranular transformation. However, under low-temperature rolling process, austenite grain boundaries remarkably increased and promoted massive PF nucleation in AL–cr steel plate, as shown in Fig. 5c.

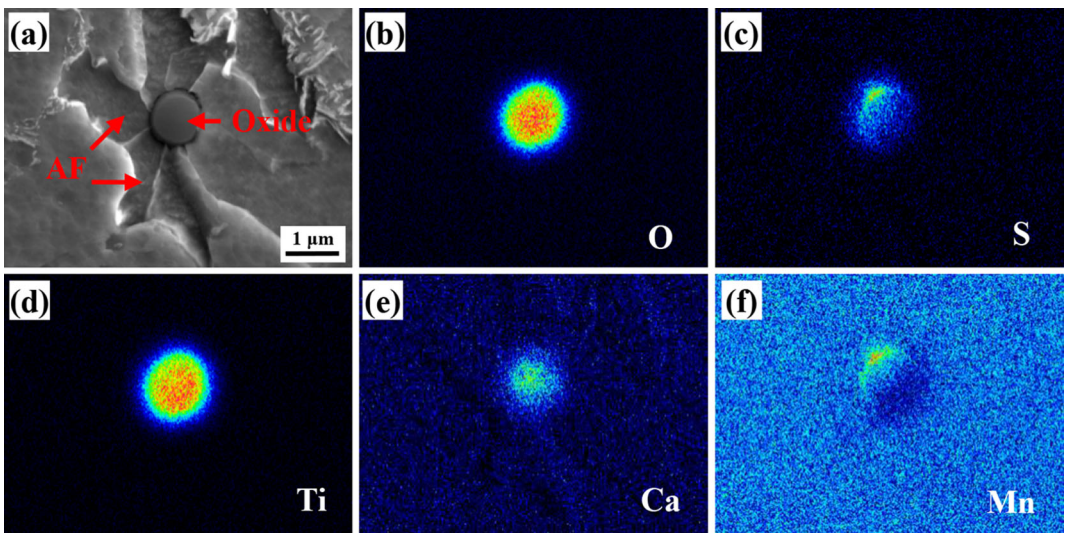

Fig. 3 Elements distribution of an oxide particle nucleating acicular ferrite in TC steel analyzed by SEM

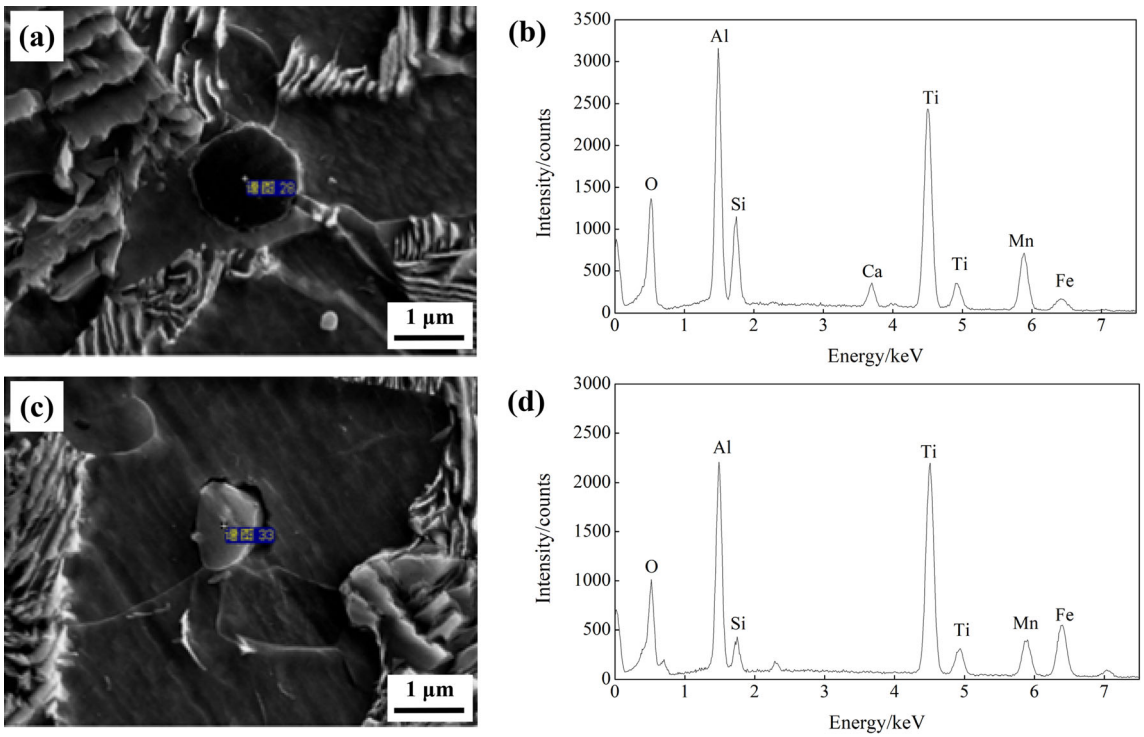

Fig. 4 Al–Ca–Ti oxide particle (**a**, **b**) and Al–Ti oxide particle (**c**, **d**) observed in experimental steel

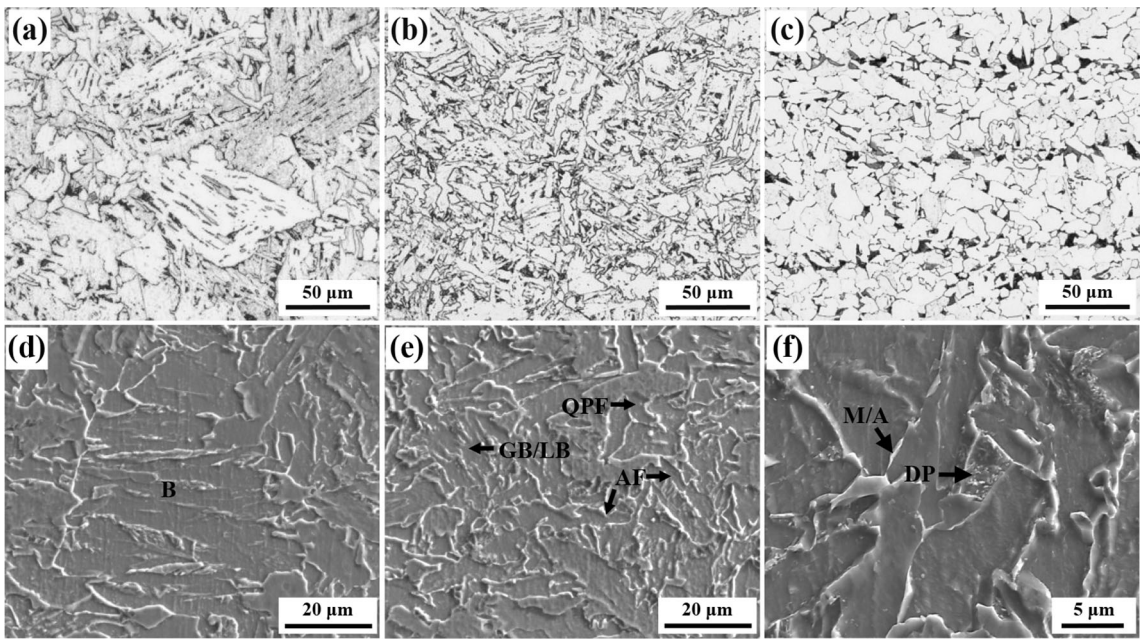

Fig. 5 Optical (**a**–**c**) and SEM (**d**–**f**) microstructures of as-rolled AL steel (**a**, **d**), TC steel (**b**, **e**, **f**), and AL–cr steel (**c**)

Mechanical properties of as-rolled steel plates are presented in Fig. 6. AL–cr steel plate had lowest tensile strength and highest impact toughness. AL steel plate had higher strength, but the toughness deteriorated to a large degree. TC steel plate achieved the highest strength and relatively good toughness. Acicular ferrite is a type of bainite that nucleates intragranularly. From the aspect of grain refinement strengthening, the effective grain size for AF structure approximately corresponds to AF lath width, whereas for bainite structure, the packets act as effective grains. Thus, strength of TC steel plate increased compared with AL steel as a result of grain refinement. The

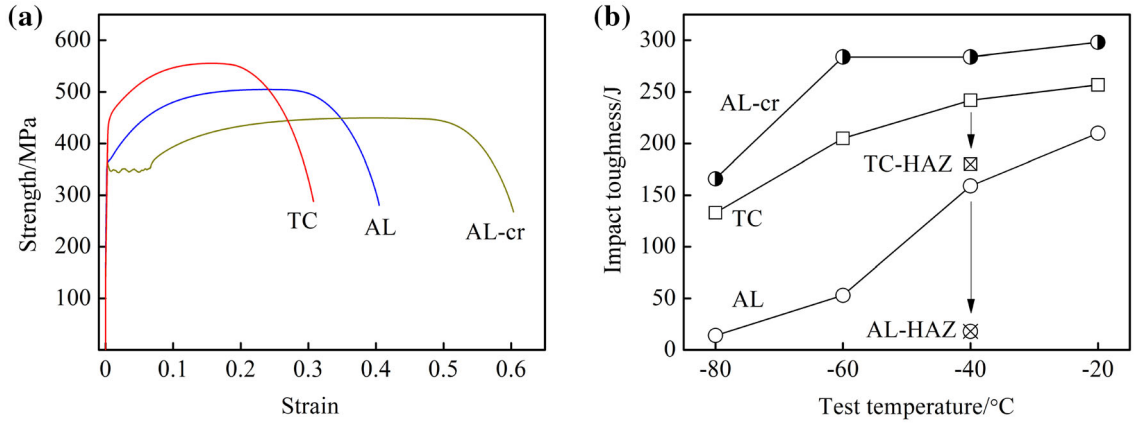

Fig. 6 Tensile curves (**a**) and impact toughness (**b**) of as-rolled steel plates

dislocation density, especially mobile dislocation, was relatively high for AF or bainite and caused continuous yielding of TC and AL steel plates. However, for AL–cr plate, the high fraction of polygonal ferrite which was low in dislocation density gave rise to a significant yield plateau [31]. Impact toughness of TC plate was also improved as a result of grain refinement compared to that of AL plate. Under conditions of similar chemical composition and microstructure type, high-angle grain boundary density is a determining factor influencing toughness. Grain boundaries of misorientation angle $> 15°$ act as effective obstacles to crack propagation. EBSD analysis in next section showed that boundaries between AF plates were high-angled, while in AL steel, high-angle boundaries only existed between coarse packets. As shown in Fig. 7a, b, impact fracture of TC plate consisted of dimpled ductile part and quasi-cleavage fracture, where the sizes of small dimples and cleavage facets were similar to the size of intragranular AF or GB/LB. Fracture of AL steel plate was all brittle cleavage type (Fig. 7c), and the coarse cleavage facet size was corresponding to that of bainite packet or prior austenite grain.

Toughness of simulated coarse-grained HAZ of two steels both decreased compared to as-rolled plates, and the impact values are also presented in Fig. 6b. The value of TC steel HAZ still kept a relatively high level, while AL steel HAZ showed serious brittleness. HAZ microstructures are shown in Fig. 8, where micrographs of Fig. 8c, d are taken from cross section of impact fracture. Bainite sheaves or ferrite side plates dominated AL steel HAZ with an even coarser size (Fig. 8a). This caused longer distance propagation of impact crack in the common cleavage plane of ferrite sheaves (Fig. 8c). TC steel HAZ obtained interlocking AF microstructure (Fig. 8b) similar to that of continuous cooling transformation product without deformation (Fig. 2f). However, its laminar GBF increased in comparison with that in Fig. 2f even though their cooling rates were similar. With the high HAZ peak temperature, nitride or sulfide particles tended to dissolve. The number of particles on austenite grain boundaries which acted as nucleation sites decreased. This induced rapid growth of ferrite along boundary and resulted in a large-sized two-dimensional structure, as indicated in the lower part of Fig. 8d. Impact crack tended to propagate directly along GBF due to its similar crystallography orientation, but it would be arrested when proceeding to the intragranular AF region, as indicated in the upper part of Fig. 8d. These factors led to decrease in toughness while still keeping a relatively good level.

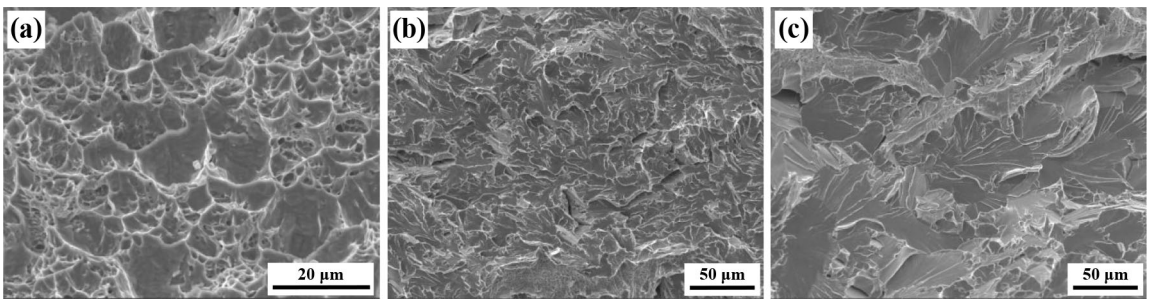

Fig. 7 SEM fractographs from − 60 °C impact sample fracture of hot-rolled TC steel (**a**, **b**) and AL steel (**c**)

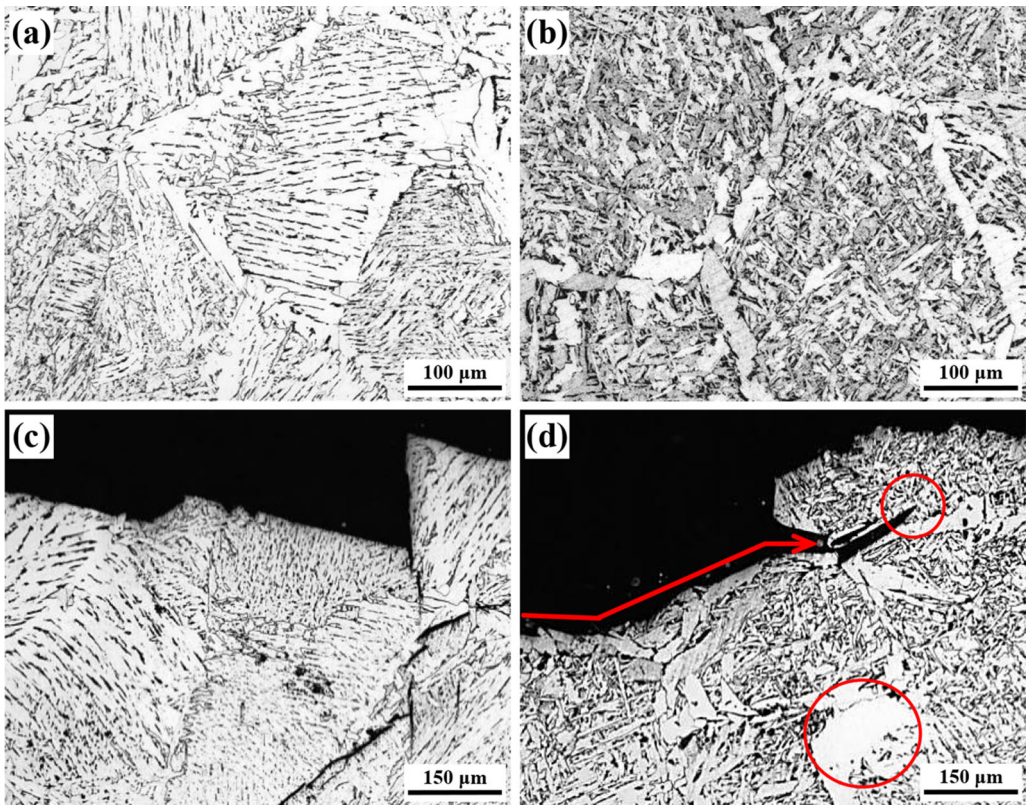

Fig. 8 Simulated coarse-grained HAZ microstructures of AL steel (**a**, **c**) and TC steel (**b**, **d**)

3.3 EBSD analysis

Microstructural evolution and its relationship with mechanical properties were studied in combination with EBSD analysis. EBSD maps of as-rolled and simulated HAZ samples are shown in Fig. 9. The image quality (IQ) map and inverse pole figure (IPF) map were made according to Kikuchi band quality and crystal orientation, respectively. High-angle (> 15°) and low-angle (5°–15°) boundaries were also drawn in IQ and IPF maps. The local misorientation map, or kernel average misorientation (KAM) map, was made through evaluating the misorientation of a pixel to its neighbors and coloring the pixel according to the degree of the misorientation. Grain boundaries > 5° were neglected during calculating. KAM value could reflect the local deformation degree or dislocation density. High-angle grain boundaries were also added on KAM maps.

According to Fig. 9a, b, boundaries between PF grains in AL–cr steel plate were high-angled and the low-angle interface or intragranular substructure was much less in number. Figure 9c shows that local misorientation was low in most PF grains, which indicated low dislocation density. In TC steel plate, as shown in Fig. 9d–f, intragranular GB/LB with high dislocation density accounted for a considerable proportion. Boundaries between AF plates and GB/LB packets were mostly high-angled. Low-angle interfaces mainly distributed within bainite packets. The interiors of AF plates also showed low-angle interfaces, especially in coarsened ferrite plates. It was indicated that acicular ferrite grains adjust the crystallographic orientation slightly during their growth [32]. In comparison with as-rolled structure, the interlocking AF morphology was more developed in HAZ and misorientation between AF was high-angled, as shown in Fig. 9j, k. In general, Fig. 9f, l indicates that acicular ferrite had a relatively high dislocation density as a result of displacive transformation mechanism like bainite. It can be found that some larger-sized AF plates which formed at an early stage of transformation had low KAM value or dislocation density. At the initial transformation stage, displacive growth of AF was easy to occur with low matrix resistance. As transformation proceeded, stress in austenite matrix increased and the latterly formed AF plates had higher dislocation density. Additionally, in both hot rolling and HAZ microstructures of TC steel, there existed small-sized intragranular PF/QPF grains with low dislocation density. Its formation and effect will be discussed hereinafter. Figure 9k, l shows that laminar GBF had the same crystallography orientation, whereas polygonal GBF showed random orientation. The two types of GBF both had low dislocation density. Boundary misorientation distributions

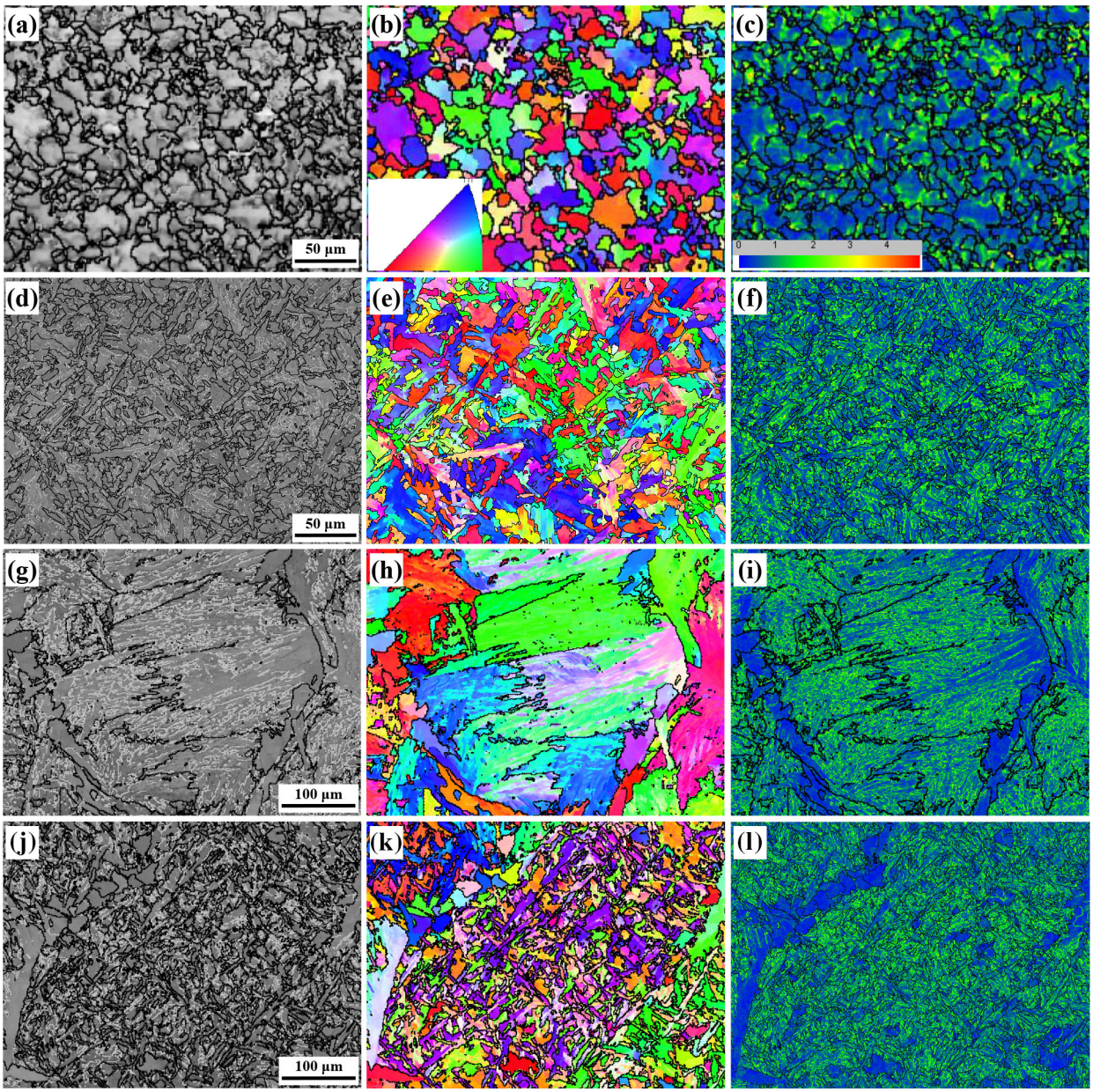

Fig. 9 EBSD maps of AL–cr steel plate (**a**, **b**, **c**), TC steel plate (**d**, **e**, **f**), AL steel HAZ (**g**, **h**, **i**) and TC steel HAZ (**j**, **k**, **l**). **a**, **d**, **g**, **j** Image quality maps with boundaries > 15° (black lines) and 5°–15° (gray lines); **b**, **e**, **h**, **k** inverse pole figure maps with boundaries > 15°; **c**, **f**, **i**, **l** local misorientation maps

of the samples are shown in Fig. 10. High-angle misorientation frequency was the highest for AL–cr steel plate, while those of TC steel plate and HAZ were similar and much higher than that of AL steel HAZ. The high-angle misorientation distribution distinctly corresponds with impact toughness shown in Fig. 6b.

In order to distinguish different grain types and characterize their substructure degree more clearly, grain orientation spread (GOS) maps were made, as shown in Fig. 11. A misorientation angle of 15° was selected to determine grain boundaries, and GOS calculation was carried out within each single grain. The average orientation of one grain was calculated firstly, and then the deviation of each pixel from that orientation was calculated. The average misorientation angle of all pixels within the grain with respect to the grain average orientation gave the average intra-grain misorientation, i.e., GOS value. Each grain was evenly colored according to its GOS value, as shown in Fig. 11. Like KAM, GOS can also reflect substructure extent or dislocation density. PF/QPF is formed through diffusional process and has low substructure degree. QPF is transformed at lower temperatures and

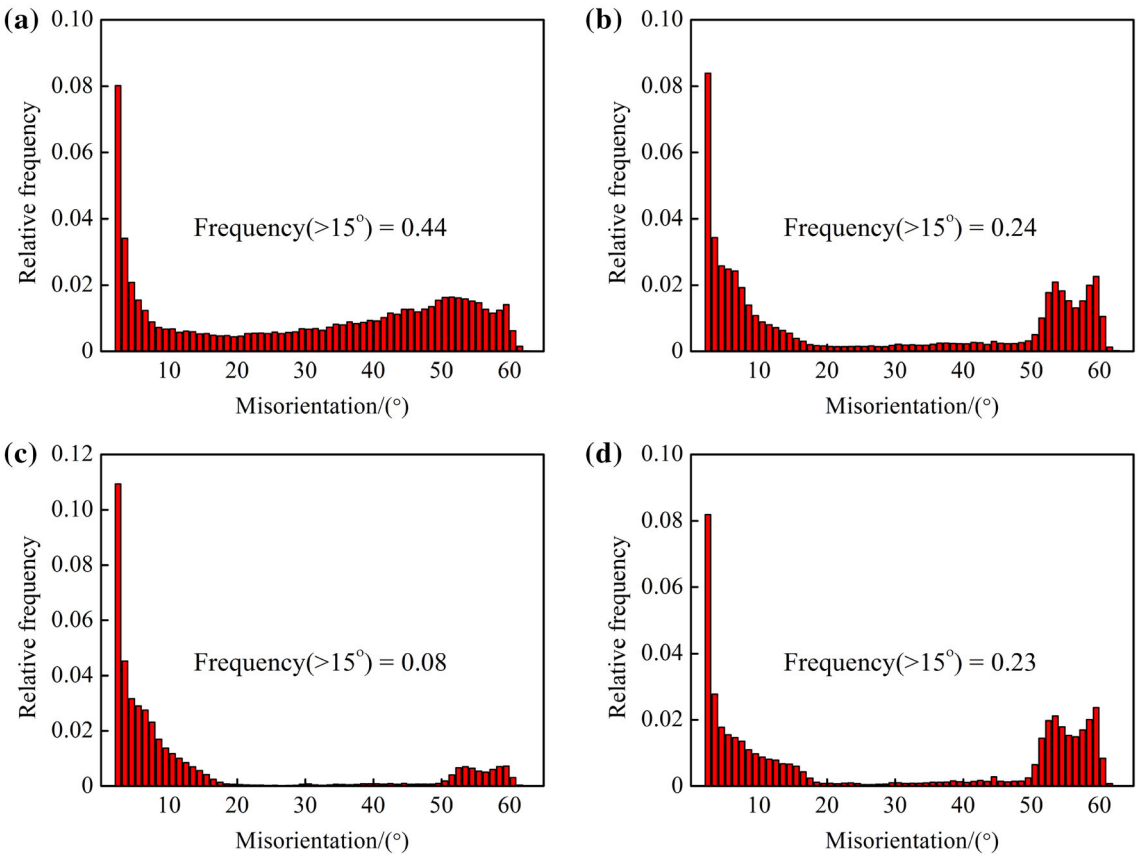

Fig. 10 Grain boundary misorientation distribution of AL–cr steel plate (**a**), TC steel plate (**b**), AL steel HAZ (**c**) and TC steel HAZ (**d**)

higher cooling rates than polygonal ferrite and has irregular grain boundaries. Grains having GOS value of 5° or smaller were classified into QPF [33], which should also include PF. Grains having GOS value > 5° were considered as AF or GB/LB here. In Fig. 11, grains in as-rolled AL–cr steel and HAZ were mostly PF/QPF and GB/LB, respectively. In TC steel plate and HAZ, area fractions of PF/QPF grains were 0.31 and 0.37, respectively, and the average grain sizes of PF/QPF in two samples were 6.2 and 7.6 μm, respectively, where grains smaller than 3 μm were neglected. In Fig. 11b, PF/QPF grains were uniform and dispersedly distributed between AF plates and GB/LB packets. For HAZ structure (Fig. 11d), fine intragranular PF/QPF grains were also uniformly distributed, whereas GBF grains were much larger. Especially for laminar GBF, even though the grain shape was not polygonal or quasi-polygonal, its substructure was not much developed and the GOS value was also < 5°. PF/QPF or GBF was considered as soft phase in comparison with AF and GB/LB. During impact fracture process, uniformly distributed PF/QPF soft phase could relieve stress concentration in front of cracks and increase crack propagation energy. However, when large-sized ferrite grains were distributed at coarse austenite grain boundaries, strain concentration was likely to occur in GBF compared with harder intragranular phase, and thus cracks tended to initiate in GBF or at the interface between GBF and intragranular hard phase. Especially in the case of laminar GBF with similar crystallographic orientation, the linear propagation of crack became much easier. Thus, under conditions of similar microstructural type and grain boundary misorientation distribution in TC steel plate and HAZ, impact toughness was influenced to a great extent by PF/QPF grains distribution.

The overall transformation process of AF microstructure was discussed in Sect. 3.1. Combined with EBSD technique, microstructural evolution of TC steel plate and HAZ can be further analyzed in detail. For hot-rolled TC steel, GBF formation was suppressed under controlled cooling process. Primary AF plates nucleated on intragranular oxide particles and were possible to grow a long distance. Secondary AF plates nucleated on ferrite/austenite interface and formed an interlocking structure together with primary AF plates. Intragranular GB/LB packets were then transformed within the divided austenite grain. During the air cooling process, carbon was able to partition from AF or GB/LB to residual austenite. Bainitic transformation would stop in carbon-enriched austenite as a result of the incomplete reaction phenomenon. With the relatively high

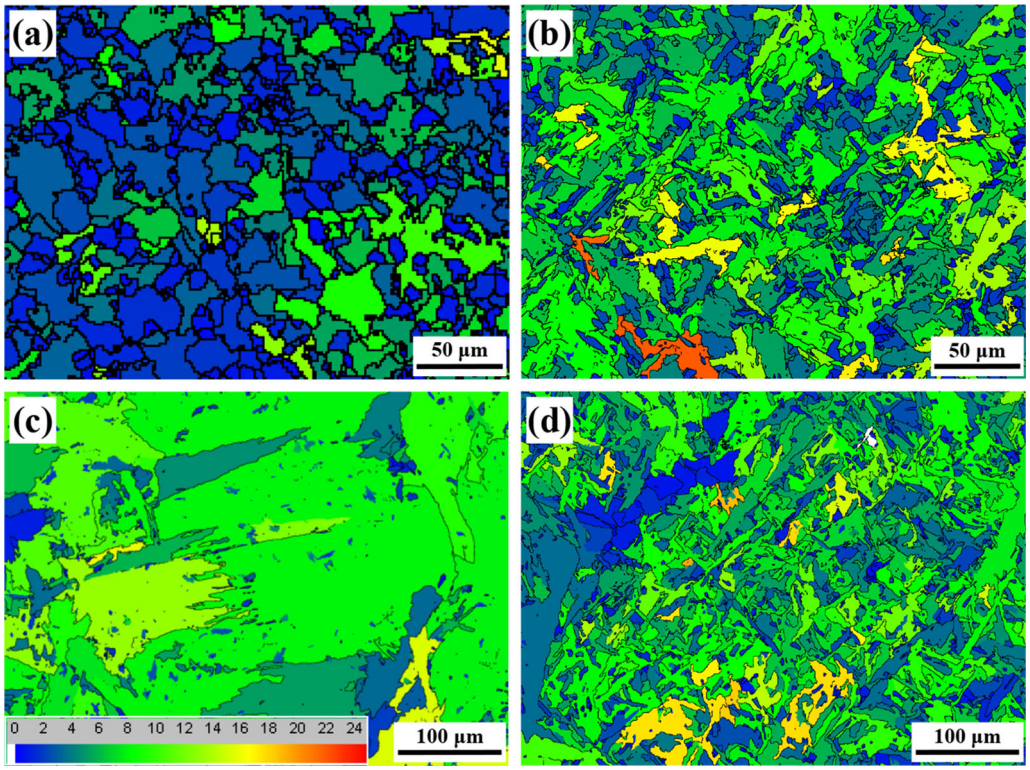

Fig. 11 GOS maps of AL–cr steel plate (**a**), TC steel plate (**b**), AL steel HAZ (**c**) and TC steel HAZ (**d**)

temperature, carbon-enriched residual austenite was then decomposed into PF/QPF and/or pearlite. A small fraction of austenite could also remain to low temperature as M/A constituent. The main evolution process can be described as AF → GB/LB → PF/QPF. By comparison, the coarse GBF formed firstly in HAZ, and intragranular GB/LB volume fraction decreased under the condition of well-developed AF structure. Thus, the HAZ microstructural evolution process can be described as GBF → AF → PF/QPF. Transformation of AF and GB/LB both satisfied K–S relationship with parent austenite.

The above results indicate that microstructure and mechanical properties of hot-rolled steel base metal can be improved by effective oxide particles combined with proper cooling process. The grain-refining behavior shows similarity to that of welding HAZ, but still exhibits some new characteristics. It also shows similar grain refinement effect to TMCP technology for HSLA steels and thus provides a promising approach for producing high-performance hot-rolled steels which are not suitable for TMCP. With the different requirements of compositions and mechanical properties for different steel products, researches on the application technology and fundamentals are still necessary to carry out.

4 Conclusion

Microstructural characteristics and mechanical properties of hot-rolled low-carbon steel containing Ti–Ca oxide particles were studied and compared with simulated coarse-grained HAZ. Oxide particles in Ti–Ca deoxidized steel were mainly Ti–Ca–O–Mn–S complex type and were effective for acicular ferrite nucleation. By the aid of dispersive particles, continuous cooling transformation products changed from grain boundary structure into intragranular types. Microstructure in steel base metal obtained under hot rolling and controlled cooling process mainly consisted of acicular ferrite and intragranular bainite, which exhibited high strength and excellent toughness. Its evolution process can be described as AF → GB/LB → PF/QPF. The resultant complex structure promoted the increase in crack propagation energy significantly. Laminar grain boundary ferrite in HAZ had similar crystallography orientation and was the main reason for toughness deterioration.

Acknowledgements This work was supported by the National Natural Science Foundation of China (U1860201 and 51904070), China Postdoctoral Science Foundation (2018M631804) and the Fundamental Research Funds for the Central Universities (N170703005).

References

[1] S.S. Babu, Curr. Opin. Solid State Mater. Sci. 8 (2004) 267–278.
[2] R. Pamnani, T. Jayakumar, M. Vasudevan, T. Sakthivel, J. Manuf. Process. 21 (2016) 75–86.
[3] C. Zhang, S. Yang, B. Gong, C. Deng, D. Wang, Mater. Sci. Eng. A 712 (2018) 430–439.
[4] H.K. Sung, S.Y. Shin, W. Cha, K. Oh, S. Lee, N.J. Kim, Mater. Sci. Eng. A 528 (2011) 3350–3357.
[5] X. Luo, Y. Niu, X. Chen, H. Tang, Z. Wang, J. Mater. Process. Technol. 242 (2017) 101–109.
[6] H. Suito, A.V. Karasev, M. Hamada, R. Inoue, K. Nakajima, ISIJ Int. 51 (2011) 1151–1162.
[7] T. Yamashita, J. Shimamura, K. Oi, M. Nagoshi, K. Oikawa, K. Ishida, ISIJ Int. 55 (2015) 2018–2026.
[8] Y. Li, X.L. Wan, W.Y. Lu, A.A. Shirzadi, O. Isayev, O. Hress, K.M. Wu, Mater. Sci. Eng. A 659 (2016) 179–187.
[9] Z. Xiong, S. Liu, X. Wang, C. Shang, X. Li, R.D.K. Misra, Mater. Sci. Eng. A 636 (2015) 117–123.
[10] J.H. Shim, Y.J. Oh, J.Y. Suh, Y.W. Cho, J.D. Shim, J.S. Byun, D.N. Lee, Acta Mater. 49 (2001) 2115–2122.
[11] T. Zhang, C. Liu, J. Qiu, X. Li, M. Jiang, ISIJ Int. 57 (2017) 314–321.
[12] C. Wang, R.D.K. Misra, M.H. Shi, P.Y. Zhang, Z.D. Wang, F.X. Zhu, G.D. Wang, Mater. Sci. Eng. A 594 (2014) 218–228.
[13] F. Chai, C.F. Yang, H. Su, Y.Q. Zhang, Z. Xu, J. Iron Steel Res. Int. 16 (2009) No. 1, 69–74.
[14] D.S. Sarma, A.V. Karasev, P.G. Jonsson, ISIJ Int. 49 (2009) 1063–1074.
[15] D. Loder, S.K. Michelic, A. Mayerhofer, C. Bernhard, Metall. Mater. Trans. B 48 (2017) 1992–2006.
[16] J.H. Shim, J.S. Byun, Y.W. Cho, Y.J. Oh, J.D. Shim, D.N. Lee, ISIJ Int. 40 (2000) 819–823.
[17] K.F. Al Hajeri, C.I. Garcia, M. Hua, A.J. Deardo, ISIJ Int. 46 (2006) 1233–1240.
[18] C. Wang, Z. Wang, G. Wang, ISIJ Int. 56 (2016) 1800–1807.
[19] X. Zou, D. Zhao, J. Sun, C. Wang, H. Matsuura, Metall. Mater. Trans. B 49 (2018) 481–489.
[20] X.D. Zou, J.C. Sun, D.P. Zhao, H. Matsuura, C. Wang, J. Iron Steel Res. Int. 25 (2018) 164–172.
[21] C. Capdevila, C. Garcia–Mateo, J. Cornide, J. Chao, F.G. Caballero, Metall. Mater. Trans. A 42 (2011) 3743–3751.
[22] T. Pan, C.F. Yang, Y. Ma, D.M. Xue, Y.Q. Zhang, J. Iron Steel Res. Int. 17 (2010) No. 3, 72–78.
[23] C. Ouchi, ISIJ Int. 41 (2001) 542–553.
[24] D. Phelan, N. Stanford, R. Dippenaar, Mater. Sci. Eng. A 407 (2005) 127–134.
[25] H. Guo, X.X. Gao, Y. Bai, M. Enomoto, S.W. Yang, X.L. He, Mater. Charact. 67 (2012) 34–40.
[26] Y.J. Zhang, K. Shinbo, T. Ohmura, T. Suzuki, K. Tsuzaki, G. Miyamoto, T. Furuhara, ISIJ Int. 58 (2018) 542–550.
[27] D.Y. Wu, F.R. Xiao, B. Wang, J.L. Liu, B. Liao, Mater. Sci. Eng. A 592 (2014) 102–110.
[28] C. Fossaert, G. Rees, T. Maurickx, H.K.D.H. Bhadeshia, Metall. Mater. Trans. A 26 (1995) 21–30.
[29] S. Terashima, H.K.D.H. Bhadeshia, Sci. Technol. Weld. Joining 11 (2006) 509–516.
[30] D.J. Abson, Sci. Technol. Weld. Joining 23 (2018) 635–648.
[31] B.M. Huang, H.W. Yen, D. Ho, H. Ho, J.R. Yang, Scripta Mater. 67 (2012) 431–434.
[32] X.L. Wan, H.H. Wang, L. Cheng, K.M. Wu, Mater. Charact. 67 (2012) 41–51.
[33] S.G. Lee, D.H. Lee, S.S. Sohn, W.G. Kim, K.K. Um, K.S. Kim, S. Lee, Mater. Sci. Eng. A 697 (2017) 55–65.